Materials Horizons

3D printing stretchable and compressible porous structures by polymerizable emulsions for soft robotics

Journal:	*Materials Horizons*
Manuscript ID	MH-COM-05-2023-000773.R1
Article Type:	Communication
Date Submitted by the Author:	26-Jul-2023
Complete List of Authors:	Bliah, Ouriel; Hebrew University of Jerusalem, Chemistry,Casali Center for Applied Chemistry, Institute of Chemistry Joe, Seonggun; Istituto Italiano di Tecnologia, Soft Biorobotics Perception Lab Reinberg, Roei; Hebrew University of Jerusalem, Chemistry, Casali Center for Applied Chemistry Nardin, Anderson; Istituto Italiano di Tecnologia, Soft Biorobotics Perception Lab; Scuola Superiore Sant'Anna, BioRobotics Institute Beccai, Lucia; Istituto Italiano di Tecnologia, Center for MicroBioRobotics@SSSA Magdassi, Shlomo; Hebrew University of Jerusalem, Chemistry, Casali Center for Applied Chemistry, Institute of Chemistry

This manuscript introduces a novel approach for fabricating 3D-printed porous structures with exceptional stretchability and compressibility, using photopolymerizable water-in-oil emulsions. What sets this concept apart from existing research is its ability to achieve both stretchability and compressibility, a rare combination in stereolithography based 3D printed hyperplastic materials. The resulting porous structures exhibit the highest reported elongation-at-break value for 3D-printed porous structures, reaching up to 450%. Moreover, they maintain excellent reversible compressibility even at 80% compression. This is made possible by the conversion of the polymerizable emulsions into open-cell structures upon printing and the subsequent removal of internal water droplets. In addition, the presented approach allows for the fabrication of high-resolution complex objects with tailored porosity, incorporating both macro-pores by design and micropores by the material's properties. The paper showcases the application in the field of soft robotics by fabricating a gripper with exceptional actuation performance, shape adaptability, and high holding force. Overall, this concept of using polymerizable emulsions for 3D printing opens new avenues for various fields of applications, including personal protection, biomedical applications, and defence. Its impact on material science, especially additive manufacturing, is expected to be profound, as the concept can be applied to a wide range of polymeric materials.

ARTICLE

3D printing stretchable and compressible porous structures by polymerizable emulsions for soft robotics

Received 00th January 20xx,
Accepted 00th January 20xx

DOI: 10.1039/x0xx00000x

Ouriel Bliah[a*], Seonggun Joe[b*], Roei Reinberg[a], Anderson B. Nardin[b,c], Lucia Beccai[b,*], and Shlomo Magdassi[a,d,*]

UV-curable 3D printing compositions for the fabrication of stretchable and flexible porous structures for soft robotics are presented. The stereolithography-based printing compositions are water-in-oil (W/O) emulsions in which water droplets are the pore-forming material, and the continuous phase is a stretchable polyurethane diacrylate (PUA). The porosity of the printed objects is controlled by the material's micro-porosity and by the macro-porosity obtained by a cellular design. The mechanical behavior can be tailored by the composition of the emulsion, providing both compliance and strength while utilizing a unique optimization methodology for fitting the ink to the 3D printer. This approach enables developing materials having superior mechanical properties, with the highest reported elongation-at-break for 3D printed porous structures, 450%. The emulsion-based printing compositions were utilized for fabricating a soft robotic gripper with unique actuation performance that could not be obtained with commonly used materials.

Introduction

Three-Dimensional (3D) printing is a technology to fabricate 3D objects, usually by layer-by-layer process, making it feasible to manufacture complex objects with high precision that can be utilized in many fields.[1] Among the 3D printing techniques, the most common are: (i) extrusion-based technologies such as fused filament fabrication (FFF) and direct ink writing (DIW); (ii) photo-curing 3D printing, such as stereolithography and Polyjet technologies; and, (iii) particles binding 3D printing, which includes Binder Jetting(BJ) and Selective Laser Sintering (SLS). In FFF, a thermoplastic melted filament is extruded through a nozzle and solidified upon cooling, while in DIW a viscous liquid is extruded through a nozzle onto a substrate to form a 2D layer[2,3]. In polyjet technology a photo-curable ink is jetted layer by layer by an inkjet printhead, followed by UV irradiation of each deposited layer. In the stereolithography method, the printing process is based on localized photopolymerization reaction within a vat filled with a photo-curable resin that solidifies upon irradiation of UV light from a laser source or digital light processing (DLP)[3] which is primarily used in this research. DLP 3D printing offers superior speed and accuracy compared to other methods, due to the instant formation of each 2D layer. Moreover, this method as shown its excellence adaptability to a range of soft materials, showing its capability to rapidly fabricate these materials into complicated 3D geometries with high resolution.[4]

One particular area where DLP of soft materials printing may realize its potential is the field of soft robotics.[4] Soft robots are generally made of flexible and hyperelastic materials that can perform smooth movements in a delicate and safe manner.[5] Soft robots can exhibit desired kinematic motions that conventional rigid robots cannot perform, such as grasping fragile or slippery objects[5] and movement in complicated terrains.[6] In general, soft actuators can be obtained by employing different actuation mechanisms, e.g., thermal,[6] magnetic, [7] electrostatic, [8] photoresponsive,[9–11] and pneumatic. [12] The mechanical performance of a soft actuator is defined by both the design and the properties of the material. Currently, there is significant interest in developing new materials for soft robotics because most traditional materials do not fully meet the necessary properties for an optimally functional and compliant soft robot. These shortcomings are primarily due to limitations in managing mechanical properties and stability, as well as restrictions in the fabrication process. [4,13,14] Moreover, while the current materials have good stretchability and

[a.] *Casali Center for Applied Chemistry, Institute of Chemistry, and Center for Nanotechnology and Nanoscience Hebrew University of Jerusalem, Jerusalem, Israel.*
[b.] *Soft Biorobotics Perception Lab, Istituto Italiano di Tecnologia (IIT), Genova, Italy.*
[c.] *The BioRobotics Institute of the Scuola Superiore Sant'Anna (SSSA), Pisa, Italy.*
[d.] *Singapore-HUJ Alliance for Research and Enterprise (SHARE), Smart Grippers for Soft Robotics (SGSR), Campus for Research Excellence and Technological Enterprise (CREATE), Singapore 138602.*

† These authors contributed equally to this work.
* Corresponding author. Email: magdassi@mail.huji.ac.il (S.M.), Lucia.Beccai@iit.it (L.B.)
Electronic Supplementary Information (ESI) available: [details of any supplementary information available should be included here]. See DOI: 10.1039/x0xx00000x

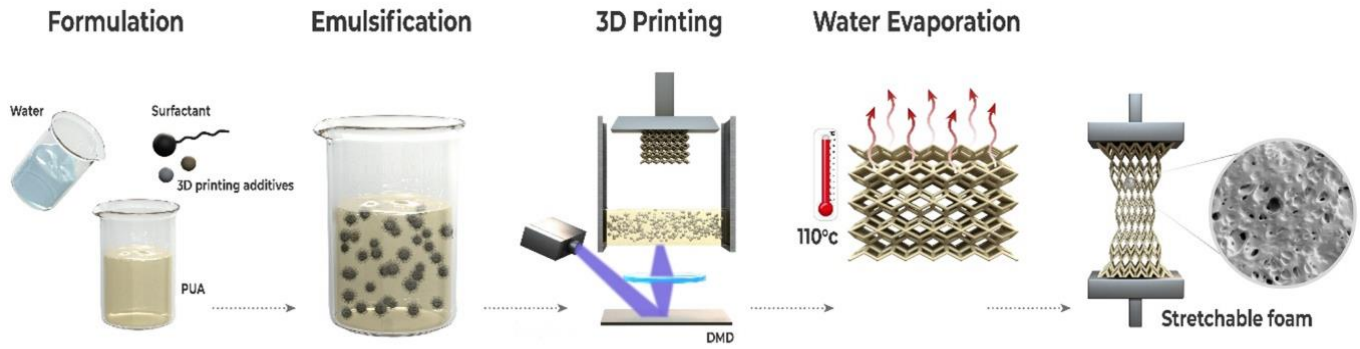

Fig. 1. Schematic illustration of 3D printing by DLP of stretchable foams from a photopolymerizable emulsion

flexibility, they are not compressible, thus limiting the shape-adaptability of the soft robot, making it a challenge to grasp delicate objects with complicated and variable geometries. Therefore, there is an unmet need for compressible and stretchable materials that can be printed at high resolution for fabricating complex structures, including those required in soft robotics.

In this research we present a detailed materials-oriented study for fabricating stretchable porous materials by water-in-oil (W/O) emulsions, based on imparting internal porosity in the printable stretchable materials, making them compressible while maintaining their stretchable nature. The most common porous materials that can be 3D printed are ceramics, metals, and polymer-ceramic composites, which are unsuitable for soft robotics due to their rigid nature. [15–25] On the other hand, polymers such as polylactic acid (PLA), high-density polyethylene (HDPE), PDMS, polystyrene (PS) and polyvinyl alcohol (PVA) can become porous by conventional processes after printing, using foaming agents or sacrificial powders. [26–32] However, these porous polymers are typically 3D printed using extrusion-based methods, which limits their structural complexity. An attractive method that can be utilized for preparing porous polymers is based on emulsion templating.[33] In this method, liquid droplets are dispersed in a medium to form an emulsion, and after one of the phases solidifies, the other is removed, thus leaving internal pores.[34] This method enables control over pore size and interconnectivity by varying emulsion compositions and it's physical parameters. Combining emulsion templating with stereolithography based DLP-3D printing, enables an additional degree of controllable porosity, by introducing macro-pores through limitless design possibilities such as hierarchical and cellular structures. Hence, further control over the mechanical properties can be achieved. [35–37] While the combination of emulsion templating and DLP printing has been explored to some extent, the field still remains largely untapped. Table S1 summarizes all the materials fabricated to date using this combination, showing that their applications rely predominantly on the high surface area such as biological scaffolds and filters. This focus is largely attributed to their rigid and brittle mechanical properties.[36–42]

In contrast, in this work we present a material that leverages the presence of internal microscopic pores with cellular structure by design to impart compressibility into an inherently stretchable matrix, thereby presenting unique mechanical properties that extends the potential and versatility of this technology to other field such as protective gears, impact resistance and soft robotics.

Furthermore, to the best of our knowledge, we present for the first-time new material compositions that enable DLP 3D printing, which results in highly stretchable porous 3D complex structures at high resolution. In addition, a detailed study on matching the developed composition to the DLP-printer is presented, including: novel solution to adhesion challenges while printing, a process for optimizing the object resolution, and the use of printing additive. The resulting 3D complex-shaped porous structures have superior mechanical properties and are demonstrated in the field of soft-robotics by fabricating soft- grippers with unique performance.

Results and Discussion

Material Development and 3D printing

The overall process for fabricating 3D porous structures by printing, is schematically presented in Fig. 1. The first step of the process is preparing a stable W/O emulsion in which the continuous phase is UV-polymerizable composition with variable fractions of water droplets. The next step is DLP 3D printing, which is based on localized photopolymerization, resulting in a stretchable polyurethane with embedded water droplets. After printing, the water droplets are removed from the structure by evaporation, resulting in an object containing microscopic pores, i.e., 3D foam, embedded within a complex structure.

In this process, we aimed at preparing a printable emulsion that is stable for at least 24 hours to ensure reliable printing without a phase separation. Initial screening of suitable emulsions was performed according to the Hydrophilic-Lipophilic Balance (HLB) classification method by Griffith. [43] In our research, the HLB of the PUA is unknown; therefore, a series of emulsions

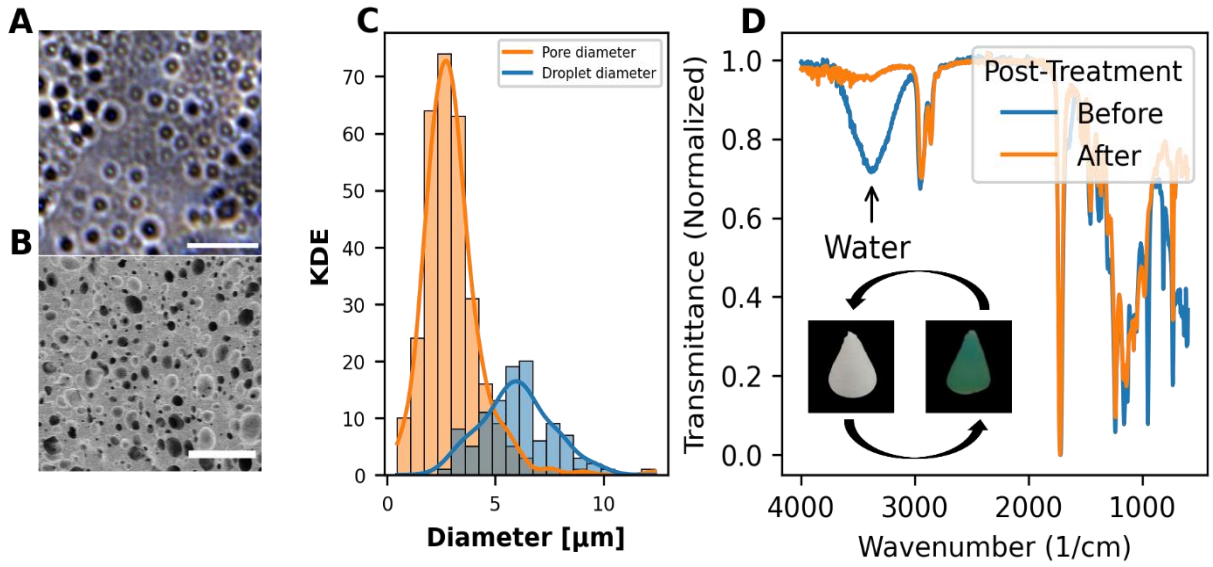

Fig. 2.: A. Optical microscope images of the unpolymerized emulsion, (scale bar 10 µm) B. SEM image of the polymerized emulsion cross section, (scale bar 50 µm). C. Comparison of droplet size distribution by kernel density estimation (KDE) of the emulsion, with the pore diameter distribution in the object after polymerization and water evaporation. D. Normalized ATR-FTIR spectrum of emulsion before and after water evaporation. The inset presents the colour of the printed cone before and after drying, in presence of CoCl2 as a moisture indicator.

using a blend of emulsifiers with a low and high HLB value were prepared at various emulsifiers ratios (emulsions containing 35 %wt water and 4 %wt emulsifiers). It was found that the best emulsion was obtained by using a blend of Span 80 and Tween 80 with a ratio of 80/20, respectively (calculated HLB of 6.4[43]). Yet, this emulsion was stable for only less than 3 hours, and therefore, we utilized an additional stabilization mechanism, which is based on steric effects. It was found that the emulsion prepared with the surfactant Pluronic L121 (PL121) showed the best stability, up to 24 hours at room temperature, until phase separation occurred.

The optimal concentration of surfactant in the emulsions was determined by measuring the droplet's size and the mechanical properties of the polymerized emulsions, as presented below.

As shown in Supplementary Fig. S1A, the droplet diameter significantly decreased from 45 µm to 3 µm while increasing the PL121 concentration from 0.5 %wt to 2 %wt, and slightly increased to droplets in the range of 3-15 µm from 4 %wt to 15 %wt respectively. In addition, it was found that the formulations with concentrations of 2 %wt and above were visually stable for at least 24 hours, thereby a reliable printing is achievable as shown in Supplementary Fig. S2-3.

To characterize the droplets in the emulsion, optical microscopy was performed on the liquid emulsions, while SEM were conducted on the polymerized emulsions after water evaporation for pores characterization as shown in Fig. 2A-B, respectively. Image analysis of these photos was performed by pore/droplet density fraction using Kernel Density Estimation (KDE) as a function of the measured pore/droplet size. As shown in Fig. 2C and D, it was found that the average pore size was 3 µm compared to the emulsion droplets size of 6 µm prior to evaporation of the water. Moreover, as shown in Supplementary Fig. S4A-C, the pores are interconnected, resulting in an overall open porous structure. This is likely to occur due to the rupture of the polymeric films by the water droplets while they evaporate.

To verify if all the water was fully evaporated, the presence of water was checked by three methods: 1) measuring the weight loss and density after the post-treatment; 2) ATR-FTIR of the emulsion before and after post-treatment (heating to evaporate the water); and 3) a visual moisture indicator (Fig. 2D inset). Overall, the weight loss of the emulsion (initially containing 35 %wt water) after post-treatment was 25 %wt, and the measured density was 1.099 g/cm3 which corresponds to 18% lower than that of the PUA without emulsification.

The water evaporation was also evaluated by measuring the presence of the OH peak by ATR-FTIR at 3380 cm^{-1} (blue and orange colour lines in Fig. 2D). It should be noted that this measurement gives information only for a thin film and not for the whole bulk structure, so it might be that there are some water droplets trapped within the structure. To address this point, a visual moisture indicator, cobalt(II) chloride, was added to the water phase of the emulsion. When hydrated, the solution colour is pink, and the cobalt salt changes to blue-green when dehydrated. A cone structure was 3D printed while the water contained the cobalt salt. As shown in Fig. 2D inset, the whole structure completely changed its colour after the post-treatment, indicating a full drying of the printed model. The colour change is reversible; by immersing the dried object in water, the object turns pink-white again due to the penetration of water to the inner part, thus confirming the interconnectivity of the pores within the structure.

To test the limits of achievable porosity, several parameters were evaluated: the range in which the emulsion is of a W/O type; the emulsion instability as a function of the water fraction; and finally, the mechanical properties of the polymerized emulsions after water evaporation.

To evaluate range in which W/O emulsions is formed, emulsions with water containing NaCl were prepared, and the conductivity of each emulsion before polymerization was measured. At low water fractions, the emulsions were not conducive, since the continuous phase is the PUA. It was found that above 55%wt water, the emulsion was conductive and therefore is of an O/W type. It should be noted that above 55 %wt water, the polymerized emulsion was not mechanically stable, and it disintegrated immediately after solidification. In addition to the conductivity measurement, the instability index of the emulsions was measured by an analytical centrifuge. Fig. 3A presents the ranges in which the emulsions are O/W or W/O type and the instability index vs. water fraction. As seen, the emulsion instability increases with the increase of the water concentration up to 25 %wt, and then the emulsion becomes more stable, until entering the O/W emulsion regime at 50 %wt water. Importantly, above 45%wt water fraction, the emulsion is too viscous for DLP printing, and therefore printing experiments were performed only up to 35%wt water content.

The mechanical properties of the printed emulsions having various surfactant and water concentrations were evaluated. The analysis was performed for sets of three tensile measurements, and the line is fitted with polynomial regression. As shown in Supplementary Fig. S1B, it was found that as the PL121 concentration increases from 0.5 to 16 %wt, the stress at break (ultimate tensile stress) decreases gradually from 0.40 to 0.15 MPa, while the strain at break is not significantly affected. Increasing surfactant concentration above 4 %wt causes a drop in the ultimate stress to less than 0.25 MPa, and the strain decreases by approximately 100%. In addition, the results for 12 and 16 %wt surfactants show only a linear behaviour, meaning that there is a loss of the elastic regime, and the curves present the strain-hardening region only, which from the practical point of view, such material behaviour is undesired because it is likely to undergo mechanical failure and therefore it tends to be unpredictable. Thus, the concentration of the surfactant for the emulsions was set at 4 %wt.

Based on this result, the printable emulsions containing varying water concentrations (ranging from 0 to 35 %wt) were characterized using tensile and compressive tests, as shown in Fig. 3B-C. The results showed that the tensile stress at break decreased significantly from 0 %wt water (PUA only-no emulsion) compared to the emulsions of PUA with different water fractions. Specifically, the stress at break decreased from 2.10 MPa to 1.05 MPa when the water fraction changed from 0 to 10 %wt, and moderately decreased from 1.05 to 0.77 MPa when increasing the water fraction in the emulsion from 10 %wt to 35 %wt. However, the tensile strain at break remained consistent at around 450% for all emulsions, similar to the PUA itself (no emulsion). The presence of water in the emulsion creates pores in the polymer matrix, which act as stress concentrators, thereby reducing the effective cross-sectional area of the material and redistributing stress within the matrix. Therefore, as the water concentration increases, more pores are formed in the polymer (Supplementary Fig. S4), and the stress is dissipated more efficiently during deformation, resulting in lower overall stress at break. These findings suggest that introducing porosity into the material can result in a softer material while maintaining its elongation at break. This feature is particularly useful in developing more energy-efficient actuators, as softer materials require less energy to deform.

Typically, commercially available rubber like polymeric materials do not allow for volumetric changes, resulting in near-incompressibility.[44,45] However, thanks to the intrinsic internal porosity that arises from the emulsion, the material allows compressibility at significantly lower pressures. Fig. 3C presents the compressibility at different water content at up to 80% compressive strain. Overall, it was found that by increasing the water content, the material requires less pressure to allow for volumetric change, and thus this approach ensures high compliance and deformability. More specifically, at 80% compression, the compressive stress gradually reduces from 4.7 MPa to 2.1 MPa when the water content increases from 0 %wt to 35 %wt, respectively. Noteworthy, at approximately 2 MPa, all the formulations undergo an internal failure. However, increasing the water content from 0 %wt (no emulsion, failure at 55% strain) to 35 %wt, the failure occurs at a significantly higher strain of 75%. Moreover, as shown in Supplementary Fig. S6 (cyclic compressive tests at 80%), it is identified that this internal failure occurs in the first cycle only, and the material remains reliable for the subsequent cycles.

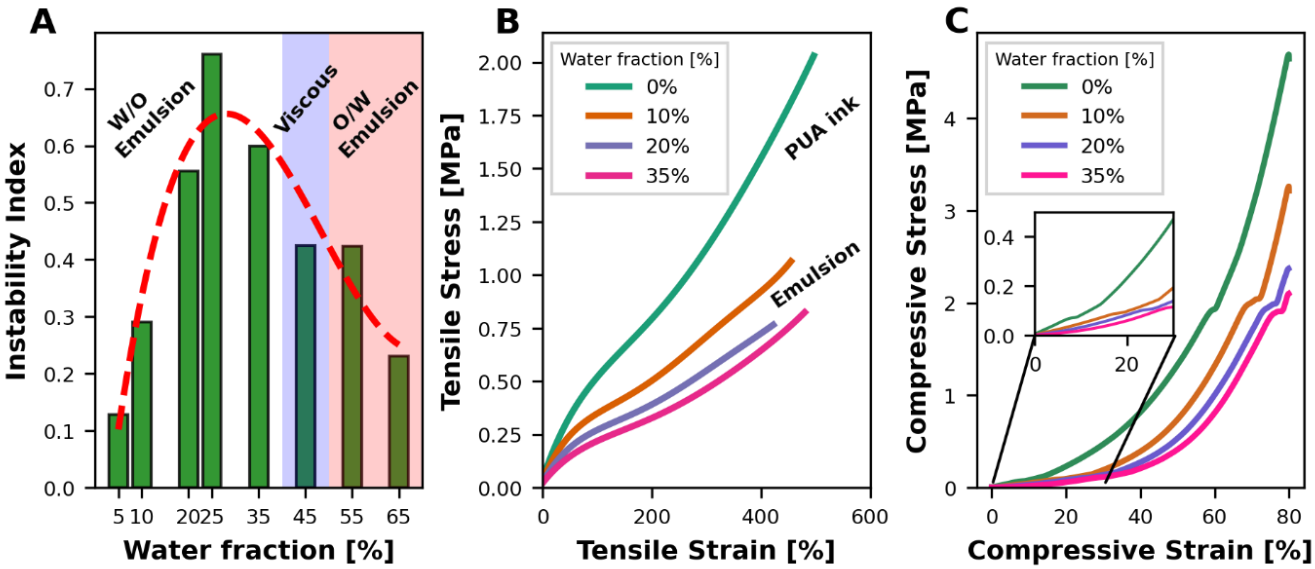

Fig. 3. A Instability of emulsion ink in various water concentrations; up to 35%, the emulsion is too viscous to be printed, and above 50%, the emulsion is O/W type. B. Regression plots based on sets of three tensile tests of different printable water concentrations. C. Compressibility test at 80% of dogbones printed with emulsions with various water concentrations, the data present the loading only of a load-release cycle, the full cycle is presented in Supplementary Fig. S5 ,the inset plot presents the first 30% compressive strain.

From a mechanical point of view, two essential characteristics should be further investigated in order to be applied in soft robotics applications. The first is to verify the repeatability, and the second is the adequate operation ranges identifying the reversible compressibility, which corresponds to strain in which the material can fully recover. In the inset plot of Fig. 3C, it is shown that for all the emulsion-based samples, the compressive strain increases linearly up to 30% strain, which means that the material exhibits structural deformability mainly due to the compression of the internal micropores. This is contrary to the PUA printing composition (0% water, not emulsion), which shows an exponential increase in compressive stress. Therefore, the operation range can be up to 30%, and the reversible compressibility can be up to 20%, which corresponds to a particular strain range that the stress response is likely to show linear behaviour concerning imposed compressive strain. As shown in Supplementary Fig. S7, there is practically no deterioration in mechanical properties during the measurements, which indicates that high reliability can be accomplished.

Finally, the shrinkage of the objects upon drying was evaluated by measuring the width of each face of a 3D printed 1 cm^3 cube, before and after post-treatment. It was found that the shrinkage is isotropic, with an average 7 % linear shrinkage of each face, and an overall volumetric shrinkage of 20%.

Optimization of the emulsion for 3D-DLP printing

The development of 3D printing process requires matching the printing compositions to the printing technology. For the DLP printing, the most important factors are the ink viscosity and stability, polymerization time, and compatibility with the printer components. The last requirement is related to obtaining, on the one hand, adhesion to the printing platform while avoiding sticking to the vat window, which is composed of transparent FEP film (fluorinated ethylene propylene). These challenges were addressed by implementing a PUA layer for better adhesion the build platform, and then introducing a silicone-based surfactant to the ink composition to lower surface tension. A more comprehensive explanation of the methods and results, including stability tests and adhesion force measurements, are provided in the Supplementary Information section 6.

In general, DLP printing of dispersed systems is particularly challenging due to the significant light scattering caused by the dispersed phase. In this study, the average droplet size in the emulsion is 6 µm, which result in high light scattering, causing undesired polymerization in non-targeted areas (overcuring). To overcome this issue, two approaches were employed: the inhibition of photopolymerization through radical scavenging using 0.005%wt hydroquinone (HyQ), and the prevention of unwanted photoinitiator activity by adding a UV absorber, Sulforhodamin B (SolB) at 0.03%wt, which competes with the photoinitiators.

Four formulations were prepared to test the validity of the approach, one without HyQ and SolB, the second containing both, and two containing each separately. The printing performance of the formulations was evaluated for 3D printed pillars having different widths, starting from the minimal printer pixel size of 62 µm, up to 500 µm, as shown in Fig. 4A-B. It was observed that below the width of 300 µm, the material was not mechanically stable, resulting in torn (below 150 µm) or crooked (200-300 µm) pillars. Therefore, the pillars with a width of 350 µm were selected for evaluating the resolution, which is determined as the ratio between the dimension of the planed and the printed object. For our purposes a ±0.05 deviation from planned dimension is the threshold for good resolution.

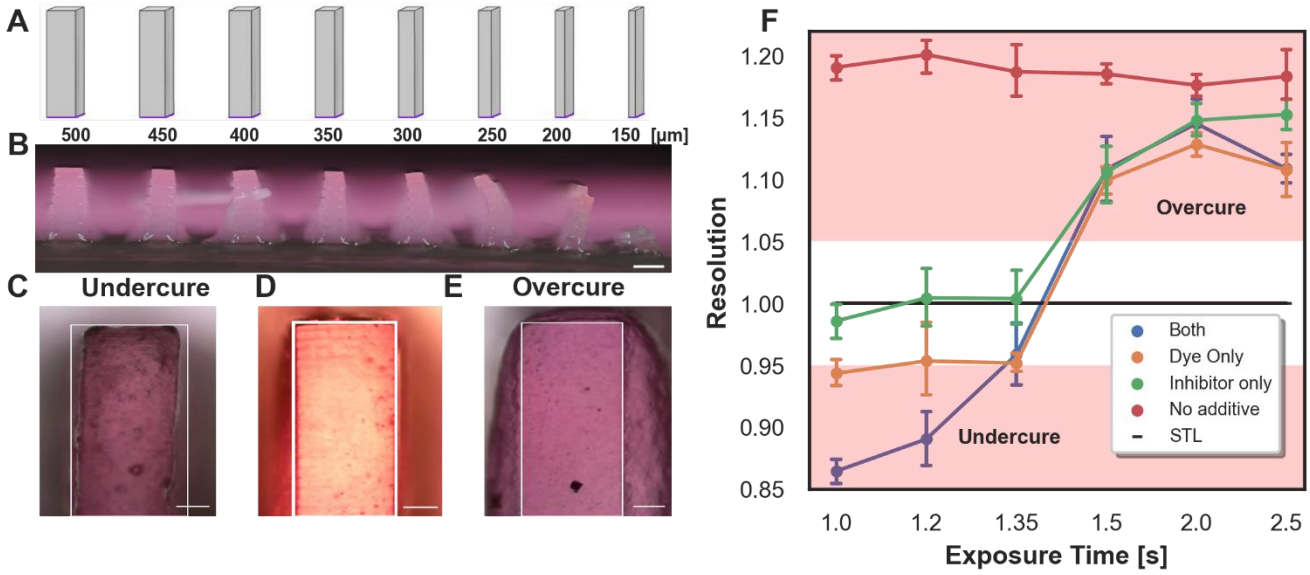

Fig. 4. Parameters affecting the printing performance. A. STL representation of the pillars for evaluating the resolution. B. Photograph of the pillars in different widths ranging from 150 to 500 µm (scale bar is 500 µm), C-E.Photograph of 350 µm pillars of formulation containing both HyQ and SolB at 1, 1.35 and 2 seconds exposure times, the white rectangle represents the dimensions of the original STL file(scale bar is 100 µm) , F. Effect of addition of HyQ and SolB on printing resolution.

In Fig. 4C-E, we compared the dimensions of the 350 µm pillar, with the size in the original STL file (marked in white frame) by measuring the actual width at different exposure times. For low exposure times (<1.2 sec), the measured size is smaller than the projected STL file, resulting in under-cured pillars (Fig. 4C), meaning that the polymerization was not completed. On the contrary, when over-irradiating (>1.5 sec), the pillar's actual size is significantly larger than that in the STL file (Fig. 4E), meaning that over-curing occurs. Fig. 4F shows more specifically the resolution as a function of the exposure time of the four above mention emulsions (with and without additives). For the formulation without any additives, the printed pillars over-cured with a poor resolution of 1.2, independent of the exposure time. This poor resolution was dramatically improved with the formulations containing HyQ and SolB, enabling high-resolution prints and pinpointing the exposure time to the range of 1.2 to 1.4 seconds. This finding was supported by the evaluation of the double bond conversion (DOC) as a function of the exposure time by following the acrylate (C-H and C=C stretching peaks) at 808 and 1407 cm^{-1} respectively, relative to the constant C=O from the carbonyl peak at 1720 cm^{-1}. [12] As shown in the green and yellow areas in Supplementary Fig. S12. It was as found (Supplementary Fig. S13) that at an exposure time of 1.35 seconds and above, up to 85% conversion is achieved, which is considered to be fully polymerized for free radical polymerization.[46]

State of the art and soft robot demonstration

After establishing the material's compositions and the major factors affecting its printability, an object with a complex structure was 3D printed to demonstrate the material capabilities. As presented in Fig. 5A-B and Supplementary Video 1, the object is constructed from a unit cell of a Buckyball-type structure with 6 hexagons and 4 squares that are arranged in a 4X2 array. As shown in the video, the structure is very stretchable and can be easily deformed by twisting, compressing and stretching, with a rapid and full recovery (i.e., high resilience) of the structure.

Our printed foams were compared with the literature reports for foams that were 3D printed by various technologies (Fig. 5C)[15,16,21–24,26,27,30–32,39,47–53] to construct the plot, we searched publications under the keywords "3D printing", "foams" or/and "porous", and evaluated only the papers that contained tensile measurements. It should be noted that most publications on photopolymerization-based printing of foams/porous materials result in stiff polymers[37,54] or ceramics[55–57] that cannot elongate and therefore tensile measurements were not reported for. As shown in Fig. 5C, most of the porous objects are fabricated by materials that are not UV-curable, thus limiting their fabrication methods to low-resolution extrusion-based 3D printing (DIW, FFF) or powder-based printing (Binder jetting (BJ) and Selective laser melting (SLM)). To the best of our knowledge, our approach presents the first stereolithography-based 3D-printed stretchable porous objects, having such high value of elongation at break.

As the stretchable porous structure exhibits superior mechanical properties and high printing resolution, it holds potential for use in pneumatic soft robots.[58] Therefore, ensuring the material is airtight is crucial for its practical implementation. Therefore, we conducted an airtightness test on a 3D-printed balloon, as presented in Supplementary Fig. S14A-D. The test involved applying a pressure of 12 kPa to the balloon and closing the pneumatic line to detect any air leakage from the balloon. As shown, the pressure remained stable over a long period,

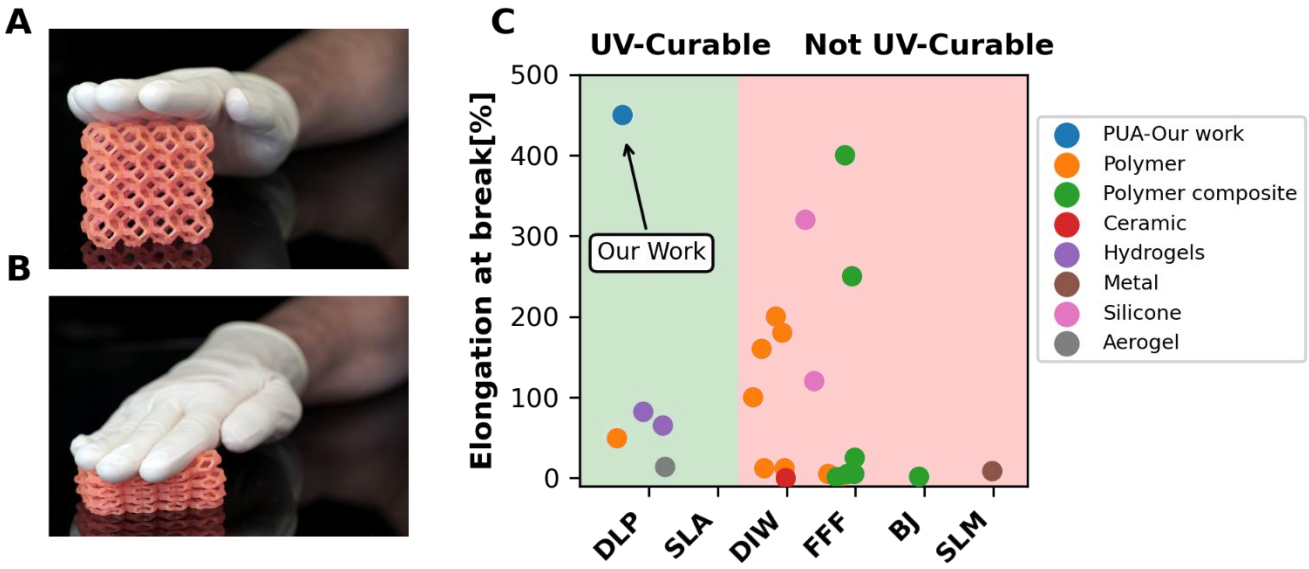

Fig. 5. 3D printed foams with complex structure before(A) and after compression(B) C. Comparative plot of various 3D printed foams classified by the 3D printing methods and materials type.

indicating that the material is suitable for soft pneumatic actuators, because their actuation time is in the seconds timescale. This finding is surprising because of the open-pore structure, which could lead to air leakage. However, as supported by the SEM images in Supplementary Fig. S15, the surface of the material is practically closed, compared to the pores seen in the cross-section. These findings can be attributed to the post-cure process, that involved the use of solvent that most probably cause the pores closure, ensuring the material's airtightness.

To demonstrate the potential capabilities of the developed material, a unique soft actuator was designed. This valve-like actuator (VLA) aims to achieve a fully monolithic structure composed solely of one material, the emulsion ink, and was designed consisting mainly of radial chambers and an elastic lattice layer attached to the internal membrane, as shown in Fig. 6A-B. The former plays a vital role in allowing the VLA to grab, hold, and support objects by implementing a force closure, i.e., due to friction, the holding force is determined by the initial compression force.[59] On the other hand, the latter enables effective grasping via a highly compliant and adaptable structure. The result is a form closure gripper with a particular morphology, similar to the fin-ray gripper[60] or the jamming-based gripper.[61]Hence, the VLA can grasp through the expansion of the internal wall upon positive pressure, while ensuring compliant and safe interaction with the object (see Fig. 6B). Thus, it is noted that these unprecedented achievements at designing a new gripper are mainly attributed to hierarchical porosities at micro and macro (i.e., mm) levels. Indeed, the presence of microporosity at the material is important to allow the lattice layer to accommodate both tensile and compressible strains. Moreover, it is also remarkable that the lattice layer allows the object to be fully engaged through an enlarged contact surface upon positive pressure imposed. Once the imposed pressure decreases down to atmospheric pressure (null phase), both chamber and lattice layers are released, and the object is then freed.

Given the printing volume of the printer used in this study, the overall dimension of the VLA was up to 36 mm in diameter and 50 mm in length. Based on this, parametric optimization was performed to maximize the deformation ratio of the internal wall, which plays a vital role in engaging the object. The parameters employed for the optimization are shown in Supplementary Fig. S17. The maximum deformation ratio of the internal wall was obtained for an offset distance of 1.8 mm and a wall thickness of 2.2 mm. A 4 mm thick lattice layer (with grid tessellations) was designed, having two 1 mm unit cells (with 1 mm pillar diameter) in the radial direction.

Finally, at atmospheric pressure (null phase), the VLA has a grasping area of about 150 mm^2 (14 mm in diameter) and it can be fully closed at 10 kPa (see Fig. 6C, Supplementary Video 2). It is remarkable that due to the tessellated structure and optimized dimension, the VLA is capable of grasping tiny objects, like a 23G needle (only 0.64 mm in diameter), as shown in Fig. 6D and Supplementary Video 3. Also, its payload corresponds to 12 times its weight; As shown, the VLA weights merely 30 g, it can lift a weight up to 350 g (Fig. 6E and Supplementary Video 4). To show the effect of the porosity, a VLA made of PUA only (0%wt water) was fabricated and a comparative analysis with the actuator made of emulsion composition (35%wt water) was made. As shown in supplementary fig. S18, there is a significant difference in the control of the closing gripper. The presence of microporosity enabled lower activation pressure, and a more linear response thus better controllability, allowing the gripper to perform more accurate movements. To summarize, the porosity is contributing to actuator in two key factors; The first, by increasing the contact surface between the object and the gripper while maintaining a strong hold through positive pressure. Second, by accommodating the bi-axis deformation

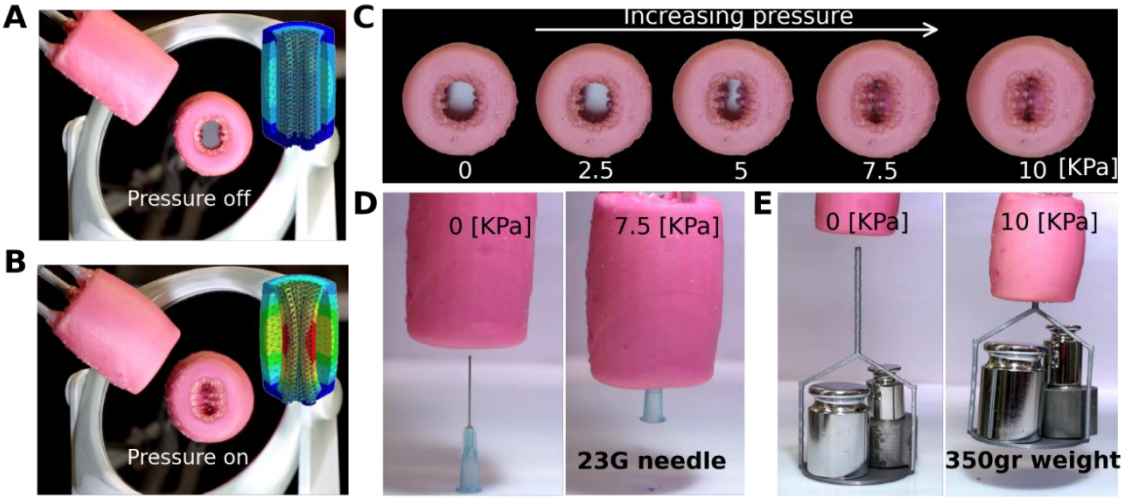

Fig. 6. Valve-like actuator (VLA) at rest (A) and activated at 7 [kPa] (B), the actuator is photographed with a reflection by a mirror, to show the internal actuation C. VLA actuation states as a function of the applied pressure. D-E. Representative demonstration of the VLA for gentle and precise grasping of a 23G needle (D), and loading of a heavy, 350 g weight (E)

(i.e. both compressive and tensile strains) that is applied by positive pressure.

Conclusions

In conclusion, this work presents a novel approach to fabricate deformable porous structures by Digtial Light Processing (DLP) printing based on using a UV-curable water-in-oil emulsions, and demonstrates its high potential for applications in the field of soft robotics.

This emulsion enables the creation of highly stretchable and compressible porous structures with controllable mechanical properties that can be tailored by simply changing the dispersed phase fraction of the material. Our research not only highlights the potential of this new compositions to drive innovations in the soft robotic field but also opens up exciting possibilities in other fields such as personalized protecting gears that require hyperelastic materials.

Experimental Section/Methods

Printing materials preparation

The emulsion continuous phase is typically composed mixture of aliphatic polyurethane acrylate (Ebecryl 8413, Allnex) and epoxy aliphatic acrylate (Ebecryl 113, Allnex) at a 1:1 weight ratio. To make the mixture photo-reactive, the photoinitiators 1-Hydroxy-cyclohexyl-phenyl-ketone (Igracure 819, BASF) and Bis(2,4,6-trimethylbenzoyl)-phenylphosphineoxide (Igracure 184, BASF) at a 1:2 weight ratio respectively were dissolved in the monomers at a concentration of 2%wt of the continuous phase.

The dispersed phase is Triple Distilled Water (TDW) at different phase fractions, ranging from 0 to 35%wt of the total emulsion. Pluronic® L-121(PL121) (Sigma Aldrich) was used as an emulsifier at different concentrations ranging from 0.5-16%wt. The additives improving ink resolution are Sulforhodamine B sodium salt (BioReagent, Sigma Aldrich) was used as a dye, Hydroquinone (99%, Sigma Aldrich) as an inhibitor, and ABIL EM 90 (Evonik) to decrease the adhesion to vat bottom film. The optimal concentrations of these additives are 0.005%wt, 0.03%wt, and 1%wt, respectively. To prepare the emulsion, the dispersed phase was dropwise added to the continuous phase containing the photo-initiators and additives, while mixing with Dispermat mixer at 4000 rpm for 8 minutes, finally, ABIL90 was added and the emulsion was de-bubbled using thinky mixer.

Digital Light Processing 3D printing

The 3D printing is conducted by Asiga MAX X35UV Digital Light Process (DLP) printer (ASIGA, Australia). Typically, the printing is performed at 0.2 mm layer thickness with 1.2 seconds UV irradiation at λ = 385 nm. After printing, the objects are rinsed with acetone and water, followed by post-curing under UV light (365 nm) for 15 minutes. Finally, to create the micropores, the water is evaporated by heating the object at 110 ^{o}C for 1 hour.

Adhesion force measurement setup

To measure the adhesion force of the first printing layer to the vat button a self-design setup was made. The rationale for the design is to simulate the process of a single layer printing where the descending of the platform and layer formation are performed by the printer, and the upraising is undertaken by the force measurement instrument (Instron4500). The setup includes a platform adapter to the printer, a printing platform with connections to Instron, a vat adapter to Instron, and a vat comprising of two parts a base and a holder that holds the vat and prevents it from moving while measuring (See Supplementary information Section 6)

Experimental measurement setup

The mechanical parameters were measured by performing a tensile test for 3D printed/photo-cured dog bones samples (ISO-527A-5A) with a Universal Testing Machine (model Instron 4500, Instron, USA) having a 500N load cell, tension rate of 10mm per minute, and an initial distance of 20mm between

grippers. ATR (Attenuated Total Reflection)-FTIR measurements were performed by Shimadzu IRPrestige-21, the spectra from Fig. 2D was normalized relative to the carbonyl peak at 1600-1900 cm^{-1}. Emulsion stability was measured by LUMiFuge analytical centrifuge at a wavelength of λ = 865 nm at 4000 RPM (5.54 times earth acceleration-g) for 24 hours. Droplet size was measured by ANKERSMID Eyetech with range A setup (0.1-300 µm). SEM images were obtained by HR-SEM Sirion. A pressure sensor (KITA-KP25C) was employed to measure the airtightness, µCT measurements were performed with EASYTOM (RX solutions) with a 150KeV source**.**

Author Contributions

O.B. and S.J. contributed equally to this work. O.B. and S.M. conceived the materials concept, L.B. and S.J. conceived the robotic design. S.M. and L.B. supervised the project. O.B. developed the material and printing procedures. S.J. designed the prototypes. O.B. fabricated the prototype. S.J. and A.N. carried out mechanical testing and analysed the data. O.B. and S.M. wrote the manuscript. S.M., O.B., S.J., and L.B. reviewed and edited the manuscript.

Conflicts of interest

There are no conflicts to declare.

Acknowledgements

This work was partly supported by the National Research Foundation, Prime Minister's Office, Singapore, under its Campus of Research Excellence and Technological Enterprise (CREATE) programme, and by the European Union's Horizon 2020 research and innovation programme under grant agreement No. 863212 (PROBOSCIS project. In addition, we thank ProFab3D for the ProFab Lattice Cube STL file which is under the Creative Commons - Attribution license(CC BY 4.0). The file was modified down from 6X6 lattice to a 4X2 lattice at a lower scale.

References

1 H. Quan, T. Zhang, H. Xu, S. Luo, J. Nie and X. Zhu, *Bioact Mater*, 2020, **5**, 110–115.

2 G. Stano, L. Arleo and G. Percoco, *Micromachines 2020, Vol. 11, Page 485*, 2020, **11**, 485.

3 Y. L. Yap, S. L. Sing and W. Y. Yeong, *Rapid Prototyp J*, 2020, **26**, 1345–1361.

4 E. Sachyani Keneth, A. Kamyshny, M. Totaro, L. Beccai, S. Magdassi, E. Sachyani Keneth, A. Kamyshny, S. Magdassi, M. Totaro and L. Beccai, *Advanced Materials*, 2021, **33**, 2003387.

5 J. Hughes, U. Culha, F. Giardina, F. Guenther, A. Rosendo and F. Iida, *Frontiers Robotics AI*, 2016, **3**, 69.

6 B. Jin, H. Song, R. Jiang, J. Song, Q. Zhao and T. Xie, *Sci Adv*, , DOI:10.1126/SCIADV.AAO3865/SUPPL_FILE/AAO3865_SM.PDF.

7 W. Hu, G. Z. Lum, M. Mastrangeli and M. Sitti, *Nature*, 2018, **554**, 81–85.

8 V. Alizadehyazdi, M. Bonthron and M. Spenko, *IEEE Robot Autom Lett*, 2020, **5**, 4679–4686.

9 J. Zhang, D. Sun, B. Zhang, Q. Sun, Y. Zhang, S. Liu, Y. Wang, C. Liu, J. Chen, J. Chen, Y. Song and X. Liu, *Mater Horiz*, 2022, **9**, 1045–1056.

10 Y. Chen, J. Yang, X. Zhang, Y. Feng, H. Zeng, L. Wang and W. Feng, *Mater Horiz*, 2021, **8**, 728–757.

11 Y. Hu, Q. Ji, M. Huang, L. Chang, C. Zhang, G. Wu, B. Zi, N. Bao, W. Chen and Y. Wu, *Angewandte Chemie International Edition*, 2021, **60**, 20511–20517.

12 D. K. Patel, H. Sakhaei, M. Layani, B. Zhang, Q. Ge, S. Magdassi, D. K. Patel, S. Magdassi, A. H. Sakhaei, B. Zhang, Q. Ge and M. Layani, *Advanced Materials*, 2017, **29**, 1606000.

13 N. Gariya and P. Kumar, *Mater Today Proc*, 2021, **46**, 11177–11181.

14 D. Rus and M. T. Tolley, *Nature 2015 521:7553*, 2015, **521**, 467–475.

15 M. A. Perras and D. Vogler, *Transp Porous Media*, 2019, **129**, 559–581.

16 C. N. Kelly, N. T. Evans, C. W. Irvin, S. C. Chapman, K. Gall and D. L. Safranski, *Materials Science and Engineering: C*, 2019, **98**, 726–736.

17 F. Zhang, Z. Li, M. Xu, S. Wang, N. Li and J. Yang, *J Eur Ceram Soc*, 2022, **42**, 3351–3373.

18 L. C. Hwa, S. Rajoo, A. M. Noor, N. Ahmad and M. B. Uday, *Curr Opin Solid State Mater Sci*, 2017, **21**, 323–347.

19 T. Ohji and M. Fukushima, *https://doi.org/10.1179/1743280411Y.0000000006*, 2013, **57**, 115–131.

20 S. Mooraj, Z. Qi, C. Zhu, J. Ren, S. Peng, L. Liu, S. Zhang, S. Feng, F. Kong, Y. Liu, E. B. Duoss, S. Baker and W. Chen, *Nano Research 2020 14:7*, 2020, **14**, 2105–2132.

21 P. Zhang, D. J. Arceneaux, Z. Liu, P. Nikaeen, A. Khattab and G. Li, *Compos B Eng*, 2018, **151**, 25–34.

22 B. Patil, B. R. Bharath Kumar, S. Bontha, V. K. Balla, S. Powar, V. Hemanth Kumar, S. N. Suresha and M. Doddamani, *Compos Sci Technol*, 2019, **183**, 107816.

23 J. E. Lee, S. J. Park, Y. Yoon, Y. Son and S. H. Park, *J Mech Behav Biomed Mater*, 2019, **91**, 193–201.

24 S. Riechmann, O. Wunnicke and A. Kwade, *Materials 2021, Vol. 14, Page 1190*, 2021, **14**, 1190.

25 P. Jagadeesh, M. Puttegowda, S. M. Rangappa, K. Alexey, S. Gorbatyuk, A. Khan, M. Doddamani and S. Siengchin, *The International Journal of Advanced Manufacturing Technology 2022 121:1*, 2022, **121**, 127–169.

26 K. Kalia, B. Francoeur, A. Amirkhizi and A. Ameli, *ACS Appl Mater Interfaces*, 2022, **14**, 22454–22465.

27 R. Abedin, X. Feng, J. Pojman, S. Ibekwe, P. Mensah, I. Warner and G. Li, *ACS Appl Polym Mater*, 2022, **4**, 1183–1195.

28 R. Woo, G. Chen, J. Zhao and J. Bae, *ACS Appl Polym Mater*, 2021, **3**, 3496–3503.

29 S. Naficy, T. Y. L. Le, F. Oveissi, A. Lee, J. C. Hung, S. G. Wise, D. S. Winlaw and F. Dehghani, *Adv Mater Interfaces*, 2020, **7**, 1901770.

30 Y. C. Yeh, L. Ouyang, C. B. Highley and J. A. Burdick, *Polym Chem*, 2017, **8**, 5091–5099.

31 T. Y. Ng, S. C. Koay, M. Y. Chan, H. L. Choo and T. K. Ong, *AIP Conf Proc*, 2020, **2233**, 020022.

32 T. Thomas, A. S. Rubfiaro, P. Nautiyal, R. Brooks, D. Dickerson, J. He and A. Agarwal, *ACS Appl Bio Mater*, 2020, **3**, 5865–5871.

33 N. A. Sears, P. S. Dhavalikar and E. M. Cosgriff-Hernandez, *Macromol Rapid Commun*, 2016, **37**, 1369–1374.

34 C. Minas, D. Carnelli, E. Tervoort and A. R. Studart, *Advanced Materials*, 2016, **28**, 9993–9999.

35 S. Limmahakhun, A. Oloyede, K. Sitthiseripratip, Y. Xiao and C. Yan, *Addit Manuf*, 2017, **15**, 93–101.

36 M. Sušec, S. C. Ligon, J. Stampfl, R. Liska and P. Krajnc, *Macromol Rapid Commun*, 2013, **34**, 938–943.

37 I. Cooperstein, M. Layani and S. Magdassi, *J Mater Chem C Mater*, 2015, **3**, 2040–2044.

38 W. J. Choi, K. S. Hwang, Y. Kim, C. Lee, S. H. Ju, H. J. Kwon, W.-G. Koh and J.-Y. Lee, *ACS Appl Polym Mater*, 2022, **4**, 1570–1575.

39 Q. Wang, Ö. Karadas, O. Backman, L. Wang, T. Näreoja, J. M. Rosenholm, C. Xu and X. Wang, *Adv Healthc Mater*, 2023, 2203243.

40 N. Sengokmen Ozsoz, S. Pashneh-Tala and F. Claeyssens, *3D Print Addit Manuf*, , DOI:10.1089/3dp.2022.0235.

41 V. Hobiger, A.-L. Kutsch, J. Stampfl, R. Liska, S. Baudis and P. Krajnc, *3D Print Addit Manuf*, , DOI:10.1089/3dp.2022.0289.

42 A. Chiappone, A. Pedico, S. Porcu, C. F. Pirri, A. Lamberti and I. Roppolo, *Polymers (Basel)*, 2022, **14**, 5265.

43 Y. Yamashita and K. Sakamoto, *Encyclopedia of Biocolloid and Biointerface Science 2V Set*, 2016, 570–574.

44 S. Joe, F. Bernabei, L. Beccai, S. Joe, F. Bernabei and L. Beccai, *Rehabilitation of the Human Bone-Muscle System*, , DOI:10.5772/INTECHOPEN.104373.

45 V. Dias, C. Odenbreit, O. Hechler, F. Scholzen and T. Ben Zineb, *Int J Adhes Adhes*, 2014, **48**, 194–209.

46 M. Moldovan, R. Balazsi, A. Soanca, A. Roman, C. Sarosi, D. Prodan, M. Vlassa, I. Cojocaru, V. Saceleanu and I. Cristescu, *Materials 2019, Vol. 12, Page 2109*, 2019, **12**, 2109.

47 R. Woo, G. Chen, J. Zhao and J. Bae, *ACS Appl Polym Mater*, 2021, **3**, 3496–3503.

48 N. Maqsood and M. Rimašauskas, *Journal of Materials Research and Technology*, 2021, **14**, 731–742.

49 C. H. Tsou, W. H. Yao, C. S. Wu, C. Y. Tsou, W. S. Hung, J. C. Chen, J. Guo, S. Yuan, E. Wen, R. Y. Wang, M. C. Sunn, S. C. Liu and M. R. de Guzman, *Journal of Polymer Research*, 2019, **26**, 1–10.

50 S. Naficy, T. Y. L. Le, F. Oveissi, A. Lee, J. C. Hung, S. G. Wise, D. S. Winlaw and F. Dehghani, *Adv Mater Interfaces*, 2020, **7**, 1901770.

51 B. H S, D. Bonthu, P. Prabhakar and M. Doddamani, *ACS Omega*, 2020, **5**, 22536–22550.

52 Y. He, F. Wang, X. Wang, J. Zhang, D. Wang and X. Huang, *Mater Des*, 2021, **202**, 109588.

53 S. H. Kim, Y. K. Yeon, J. M. Lee, J. R. Chao, Y. J. Lee, Y. B. Seo, M. T. Sultan, O. J. Lee, J. S. Lee, S. il Yoon, I. S. Hong, G. Khang, S. J. Lee, J. J. Yoo and C. H. Park, *Nature Communications 2018 9:1*, 2018, **9**, 1–14.

54 M. Sušec, S. C. Ligon, J. Stampfl, R. Liska and P. Krajnc, *Macromol Rapid Commun*, 2013, **34**, 938–943.

55 J. Guo, Y. Zeng, P. Li and J. Chen, *Ceram Int*, 2019, **45**, 23007–23012.

56 G. Qi, Y. Zeng and J. Chen, *Ceram Int*, 2022, **48**, 14568–14577.

57 Y. Fu, Z. Chen, G. Xu, Y. Wei and C. Lao, *J Alloys Compd*, 2019, **789**, 867–873.

58 S. Joe, O. Bliah, S. Magdassi and L. Beccai, *Advanced Science*, , DOI:10.1002/advs.202302080.

59 J. Y. Lee, Y. S. Seo, C. Park, J. S. Koh, U. Kim, J. Park, H. Rodrigue, B. Kim and S. H. Song, *IEEE Transactions on Industrial Electronics*, 2021, **68**, 12441–12451.

60 W. Crooks, G. Vukasin, M. O'Sullivan, W. Messner and C. Rogers, *Frontiers Robotics AI*, 2016, **3**, 70.

61 E. Brown, N. Rodenberg, J. Amend, A. Mozeika, E. Steltz, M. R. Zakin, H. Lipson and H. M. Jaeger, *Proc Natl Acad Sci U S A*, 2010, **107**, 18809–18814.

